PCCP

PAPER

View Article Online
View Journal | View Issue



Cite this: *Phys. Chem. Chem. Phys.*, 2020, **22**, 10295

# Designing an active $Ta_3N_5$ photocatalyst for $H_2$ and $O_2$ evolution reactions by specific exposed facet engineering: a first-principles study†

Moussab Harb,* Luigi Cavallo and Jean-Marie Basset

Received 12th March 2020,
Accepted 16th April 2020

DOI: 10.1039/d0cp01394c

rsc.li/pccp

The effects of native defects and exposed facets on the thermodynamic stability and photocatalytic characteristics of $Ta_3N_5$ for water splitting are studied by applying accurate quantum computations on the basis of density functional theory (DFT) with the range-separated hybrid functional (HSE06). Among the three explored potential candidates for O-enriched bulk $Ta_3N_5$ structures with substituted O at N sites and accompanied by interstitial O or Ta-vacancies, the first and third structures are relevant. The four possible (001), (010), (100) and (110) low Miller index exposed facets of $Ta_{(3-x)}N_{(5-y)}O_y$ ($y = 7x$) are also explored, which show lower formation energies than those of $Ta_3N_5$. This highlights O occupation at N sites together with Ta vacancies as native defects in the prepared samples. The most appropriate facets for HER and OER are predicted based on the redox and transport characteristics. Our work predicts (001) and (110) facets only for HER, whereas the (010) facet is predicted for OER. Our findings indicate the importance of understanding the significance of various facets when preparing and testing new material photocatalysts for water splitting reactions.



## Introduction

The production of hydrogen from water splitting using sunlight and a photocatalytic material is an attractive technology for a new future with clean energy without polluting byproducts.[1–5] Although active photocatalysts have been reported for either hydrogen or oxygen evolution reactions, a crucial challenge still remains of the possibility to achieve the two reactions simultaneously, which requires an adequate material to be found. The design of new semiconductor materials with different exposed facets is expected to give different optoelectronic and redox features directly affecting their photocatalytic performance.[6–13] For good migration of free carriers to the surface along with minimal electron/hole recombination, the effective masses are needed to be small (near that of the free electron one) along two distinctive crystalline directions.[14–16] To drive the electrons for reducing $H^+$ ions and the holes for oxidizing water, the conduction band minimum and the valence band maximum (CBM and VBM) need to be, respectively, located energetically above $H^+/H_2$ and below $O_2/H_2O$ potentials.[17] For enhancing the kinetics of electron and hole transfer to water, the co-catalysts for $H_2$ and $O_2$ evolution reactions, OER and HER, should be deposited on the best exposed facets.

Tantalum nitride ($Ta_3N_5$) is a widely used photocatalyst for solar water splitting, due to its band gap energy of 2.1 eV.[18–23] By nitrating $Ta_2O_5$ at high temperatures, $Ta_3N_5$ powder samples were obtained and the orthorhombic crystal structure was revealed by characterization techniques.[18–23] As invoked in the literature, the material could separately generate oxygen or hydrogen from water by the use of sacrificial reagents.[18,23] The overall water splitting needs to be carefully examined when using this material in order to overcome the limited efficiency. Photocatalytic measurements are related to the method of sample preparation.[20,23] This discrepancy was justified by the presence of unavoidable O impurities in $Ta_3N_5$ samples, which originated from $Ta_2O_5$ nitridation methods,[20,23] leading to defective or non-stoichiometric compounds. One should always be reminded that preparing electrodes using powder materials is not at all easy and leads to a lot of difficulties.[19] $Ta_3N_5$ flat band potentials were found to be dependent on the photoelectrode fabrication method.[23] Because $Ta_3N_5$ surfaces tend to be oxidized and the surface oxidation rate may be modified during photocatayic reactions, the expected effects of morphology (nature/type of exposed facets) together with intrinsic defects (such as O impurities and Ta vacancies) on $Ta_3N_5$ photoredox reactions need to be well understood. These aspects will be provided in this work *via* density functional theory (DFT).

*KAUST Catalysis Center (KCC), Physical Sciences and Engineering Division (PSE), King Abdullah University of Science and Technology (KAUST), Thuwal 23955-6900, Saudi Arabia. E-mail: moussab.harb@kaust.edu.sa; Tel: +966-012-8080788*

† Electronic supplementary information (ESI) available: Computational details for the different methods used in this work. Convergence tests of the electronic properties of (001), (010), (100) and (110) pure $Ta_3N_5$ slabs with crystal thickness based on the DFT/PBE method. Electronic structure of bulk $Ta_3N_5$ crystal using the DFT/HSE06 method. DFT/PBE-based metastable slab atomic structures of (110), (100), (010) and (001) partially O-enriched $Ta_3N_5$ facets. See DOI: 10.1039/d0cp01394c

In previous theoretical works,[24–30] we have studied various fundamental characteristics for solar energy conversion to chemicals with a series of materials commonly utilized in photocatalysis and reproduced with high accuracy the experimental results. This was achieved by performing first-principles computations based on density functional theory (DFT) along with the range-separated hybrid Heyd–Scuseria–Ernzerhof (HSE06)[31,32] functional. The choice of the level of theory, in particular, the chosen HSE06 functional, was previously justified based on a systematic comparison with the results obtained using the common standard GGA-PBE functional.[24–30] Using this scheme, we recently identified the most appropriate exposed facets of $TiO_2$ (in anatase and rutile phases) for photocatalytic hydrogen and oxygen evolution reactions by combining their optoelectronic and redox properties.[33] Our predicted results could successfully give rational insights into the fundamental origin behind the better activity of anatase for HER compared to rutile as found in experiments.[33–36]

In this paper, we introduce a systematic study on the impact of intrinsic defects and exposed facets on the optoelectronic and redox features of a $Ta_3N_5$ water splitting photocatalyst by applying the DFT/HSE06 method. We explored three potential candidates of O-enriched bulk $Ta_3N_5$ structures. They are associated with substituted O at N sites (unbalanced charges) and accompanied by interstitial O or Ta-vacancies for the charge balance. By selecting the most relevant bulk structures, we then carried out calculations on the thermodynamic stability, and optoelectronic and redox characteristics for the four possible (001), (010), (100) and (110) low Miler indexes of O-enriched $Ta_3N_5$ exposed facets. Moreover, we identified the most appropriate facets for OER and HER reactions and made a comparison with the three principal (023), (310) and (113) facets of prepared $Ta_3N_5$ samples. We believe that the concepts resulting from this theoretical study will guide experimentalists in selecting the most suitable exposed facets where the two HER and OER co-catalysts should be anchored for improving reduction of protons and oxidation of water.

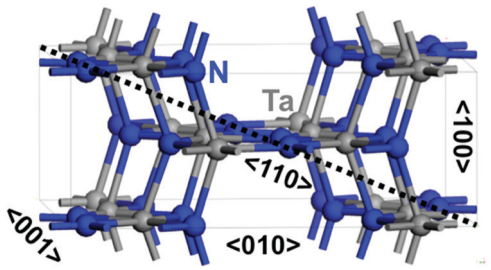


Fig. 1 Atomic structure of bulk $Ta_3N_5$ unit cell together with the four possible ⟨110⟩, ⟨100⟩, ⟨010⟩ and ⟨001⟩ crystallographic directions. Ta is shown in gray, O is shown in red, and N is shown in blue.

## Computational models and methods

### Bulk models

For bulk $Ta_3N_5$, the common orthorhombic crystal lattice with space group *Cmcm* was used (Fig. 1), as obtained experimentally using different characterization techniques.[20] To provide a good description of the required features with minimal possible errors occurring from the periodicity, we have chosen the $(3 \times 3 \times 1)$ $Ta_3N_5$ supercell containing 96 atoms ($Ta_{36}N_{60}$) for simulation rather than the unit cell (Fig. 2).

Regarding O-enriched bulk $Ta_3N_5$ structure simulation, three potential candidates were explored starting from the $(3 \times 3 \times 1)$ pure $Ta_3N_5$ ($Ta_{36}N_{60}$) supercell. Two substituted O at N sites ($Ta_{36}N_{58}O_2$), two substituted O at N sites together with one interstitial O ($Ta_{36}N_{58}O_3$) and five substituted O at N sites accompanied by one Ta-vacancy ($Ta_{35}N_{55}O_5$). The corresponding stoichiometry $Ta_{(3-x)}N_{(5-y)}O_y$ was adopted with $x = 0$; $y = 0.17$ for the first model, $x = 0$; $y = 0.25$ for the second one, and $x = 0.1$; $y = 0.5$ for the third one, respectively. For each bulk structure, many structural configurations were explored to find the most preferential O location inside the $Ta_3N_5$ lattice as well as with respect to the Ta-vacancies.

The thermodynamics of the most relevant $Ta_{(3-x)}N_{(5-y)}O_y$ bulk structures was investigated using the following reaction:

$$Ta_3N_5(s) + \frac{y}{2}O_2(g) \rightarrow Ta_{(3-x)}N_{(5-y)}O_y(s) + xTa(s) + \frac{y}{2}N_2(g) \quad (1)$$

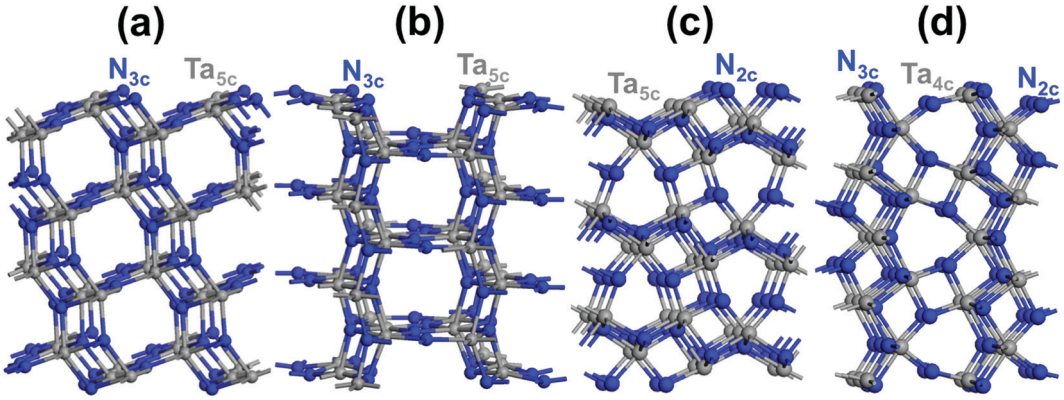


Fig. 2 Structures of the low-index pure $Ta_3N_5$ exposed facets: (a) (110), (b) (100), (c) (010) and (d) (001). Ta is shown in dark gray and N is shown in blue. In each structure, the coordination numbers of Ta and N surface atoms are highlighted.

 

The bulk formation energy relative to $Ta_3N_5$ was obtained as follows:

$$E_{\text{form}}^{(\text{bulk})} = E_{\text{e}}^{\text{Ta}_{(3-x)}\text{N}_{(5-y)}\text{O}_y} + xE_{\text{e}}^{\text{Ta}} - E_{\text{e}}^{\text{Ta}_3\text{N}_5} + \frac{y}{2}\left(E_{\text{e}}^{\text{N}_2} - E_{\text{e}}^{\text{O}_2}\right) + y(\Delta\mu^{\text{N}} - \Delta\mu^{\text{O}}) \quad (2)$$

$E_{\text{e}}^{\text{Ta}_{(3-x)}\text{N}_{(5-y)}\text{O}_y}$, $E_{\text{e}}^{\text{Ta}_3\text{N}_5}$ and $E_{\text{e}}^{\text{Ta}}$ are the electronic energies of $Ta_{(3-x)}N_{(5-y)}O_y$, $Ta_3N_5$ and pure Ta bulk materials in their lowest-energy structure, respectively. $E_{\text{e}}^{\text{O}_2}$ and $E_{\text{e}}^{\text{N}_2}$ are the $O_2$ and $N_2$ electronic energies, respectively. $\mu^{\text{O}}$ and $\mu^{\text{N}}$ are the oxygen and nitrogen chemical potentials, respectively, which are related to partial pressure and temperature by the entropy and enthalpy corrections as follows:

$$\Delta\mu^{\text{N,O}}(T,p) = \frac{1}{2}\left[h^{\text{N}_2,\text{O}_2}(T) - T\cdot s^{\text{N}_2,\text{O}_2}(T) + RT\ln\left(p^{\text{N}_2,\text{O}_2}/p_0\right)\right] \quad (3)$$

In previous combined theoretical–experimental works,[37–39] we have applied this methodology to study the thermodynamics of defective materials for photoelectrochemistry and photocatalysis and provided the results in accordance with the measured data.

### Surface models

In the case of pure $Ta_3N_5$, (001), (010), (100) and (110) low-index Miller facets were contructed using $2\times1$, $2\times1$, $1\times1$ and $1\times1$ slab models (Fig. 2), respectively. A 15 Å (001) thickness ($Ta_{36}N_{60}$ or 9 layers; $Ta_{36}N_{60}$), 15 Å (010) thickness ($Ta_{36}N_{60}$ or 9 layers), 13 Å (100) thickness (7 layers or $Ta_{42}N_{70}$) and 14 Å (110) thickness (8 layers or $Ta_{48}N_{80}$) were allowed to converge towards the bulk properties of the material, as displayed in Fig. S1 (see the ESI† for more details).

Regarding the partially O-enriched $Ta_3N_5$, (001), (010), (100) and (110) facets were modeled using the obtained optimal thicknesses of pure $Ta_3N_5$. A (110) slab model of 14 Å ($Ta_{47}N_{73}O_7$), (100) slab model of 13 Å ($Ta_{41}N_{63}O_7$), (010) slab model of 15 Å ($Ta_{35}N_{53}O_7$) and (001) slab model of 15 Å ($Ta_{35}N_{53}O_7$) were selected on the basis of the number of new sub-coordinated surface N generated upon crystal cleavage together with the most relevant sub-coordinated bulk N species generated after releasing the Ta-vacancy. These four models led to the stoichiometry $Ta_{(3-x)}N_{(5-y)}O_y$ with $x$ = 0.072; $y$ = 0.437 for (110), $x$ = 0.072; $y$ = 0.50 for (100), $x$ = 0.084; $y$ = 0.583 for (010) and $x$ = 0.084; $y$ = 0.583 for (001). For each slab structure, key structural configurations were explored by replacing with O some of the new sub-coordinated 2-fold or 3-fold coordinated surface N that appeared after cleavage and the 3-fold coordinated bulk N sites when Ta-vacancies are present inside the lattice to find the most favorable location of O.

Using reaction (1), we investigated the thermodynamics of the most relevant $Ta_{(3-x)}N_{(5-y)}O_y$ surface structures. We calculated the surface formation energy relative to $Ta_3N_5$ as follows:

$$E_{\text{form}}^{(\text{surface})} = \frac{1}{2A}\left[E_{\text{e}}^{\text{Ta}_{(3-x)}\text{N}_{(5-y)}\text{O}_y} + xE_{\text{e}}^{\text{Ta}} - E_{\text{e}}^{\text{Ta}_3\text{N}_5} + \frac{y}{2}\left(E_{\text{e}}^{\text{N}_2} - E_{\text{e}}^{\text{O}_2}\right) + y(\Delta\mu^{\text{N}} - \Delta\mu^{\text{O}})\right] \quad (4)$$

where $E_{\text{e}}^{\text{Ta}_{(3-x)}\text{N}_{(5-y)}\text{O}_y}$, $E_{\text{e}}^{\text{Ta}_3\text{N}_5}$, and $E_{\text{e}}^{\text{Ta}}$ are the electronic energies of $Ta_{(3-x)}N_{(5-y)}O_y$, $Ta_3N_5$ and Ta slab materials, respectively, in their most favorable structure with top and bottom identical terminations. $A$ represents the surface area of the slab model. $E_{\text{e}}^{\text{N}_2}$, $E_{\text{e}}^{\text{O}_2}$, $\Delta\mu^{\text{N}}$ and $\Delta\mu^{\text{O}}$ follow the same definitions as discussed in the Bulk models subsection.

## Methods

All bulk and slab structural optimization calculations were done by means of spin-polarized periodic density functional theory (DFT) with the projector-augmented wave (PAW)[40] potential and the Perdew–Burke–Ernzerhof (PBE)[41] functional using VASP software.[42–45] Thermodynamic calculations were carried out using DMol[46] software with the double numerical polarization (DNP)[47] basis set and the PBE functional. Electronic structure calculations were done using the DFT/HSE06 method with VASP based on the DFT/PBE relaxed geometries. Calculations of relative energy to vacuum were obtained from the DFT/HSE06 local potential profiles along each surface[48–53] using VASP software. Calculations of hole/electron effective mass tensors were obtained from the DFT/HSE06-based computed band structure with the VASP software using the finite difference method.[54] Details for the various computational techniques adopted in this work are presented in the ESI.†

## Results and discussion

### Atomic/electronic bulk structures and carrier transport features

The orthorhombic crystalline lattice of $Ta_3N_5$ is formed by distorted edge-sharing octahedra (Fig. 1).[20,23,26,55,56] Each Ta is linked to 3- and 4-coordinated N. The computed bulk lattice constants reproduced well the measured values[20,23,26,55,56] (Table 1).

Considering the $Ta_3N_{4.83}O_{0.17}$ material, the most favorable structure is found when the two 3-fold-coordinated N sites are replaced with O, as shown in Fig. 3a. For this structure, a

Table 1 Lattice constants (Å; °) and formation energy (in kJ mol$^{-1}$ at 1200 K) of the three potential partially O-enriched bulk $Ta_3N_5$ optimized structures

| | | | Lattice constants | | | | | |
|---|---|---|---|---|---|---|---|---|
| Material | Structure | Formation energy | $a$ | $b$ | $c$ | $\alpha$ | $\beta$ | $\gamma$ |
| $Ta_3N_5$ | Expt[20,23,26,55,56] | — | 3.89 | 10.22 | 10.28 | 90 | 90 | 90 |
| $Ta_3N_5$ | 1(b) | — | 3.89 | 10.25 | 10.27 | 90 | 90 | 90 |
| $Ta_3N_{4.83}O_{0.17}$ | 2(a) | −42.54 | 3.91 | 10.19 | 10.28 | 90 | 90 | 90 |
| $Ta_3N_{4.83}O_{0.25}$ | 2(b) | −57.62 | 3.89 | 10.23 | 10.25 | 89.68 | 90 | 90 |
| $Ta_{2.9}N_{4.6}O_{0.4}$ | 2(c) | −98.60 | 3.89 | 10.23 | 10.27 | 90 | 90 | 90 |

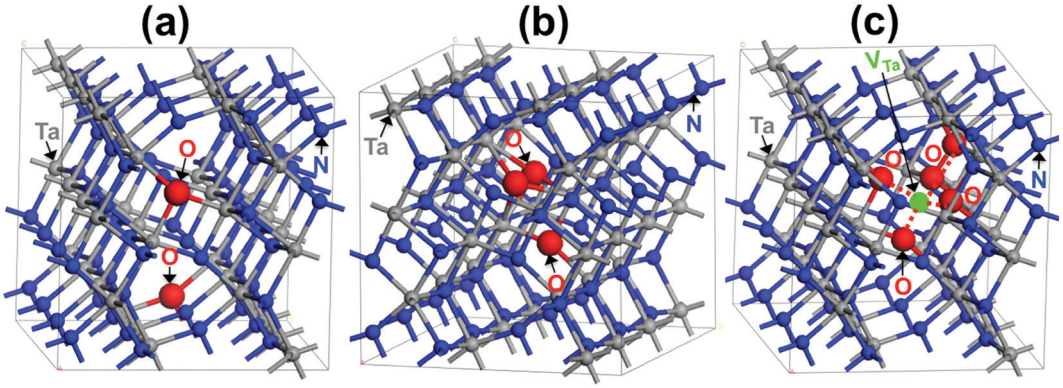


Fig. 3 Most favorable structures of the three potential partially O-enriched bulk $Ta_3N_5$ materials: (a) $Ta_3N_{4.83}O_{0.17}$, (b) $Ta_3N_{4.83}O_{0.25}$ and (c) $Ta_{2.9}N_{4.6}O_{0.4}$. Ta is shown in dark gray, O is shown in red and N is shown in blue.

singlet state associated with two extra paired up electrons in a delocalized state throughout the crystal is found to be the most favorable spin situation. The computed lattice constants are very similar to those of $Ta_3N_5$ (Table 1). The structure associated with two O occupying two 4-fold coordinated N was found to be 4.83 kJ $mol^{-1}$ less stable than that of the previous one.

Regarding $Ta_3N_{4.83}O_{0.25}$, the geometrical structure is particularly stable when the three O atoms are gathered between two Ta, forming two $TaO_3N_4$ polyhedra, one $TaO_2N_5$ polyhedron and one $TaON_5$ octahedron (see Fig. 3b). The computed lattice parameters obtained for this structure are also similar to those of pure $Ta_3N_5$, except for a small decrease in the angle $\alpha$, by 0.32° (see Table 1). In this structure, the interstitial O is located nearby the two other substitutional O, occupying two three-coordinated N bridging two Ta. The most favorable spin configuration is a singlet state, leading formally to three $O^{2-}$ defects replacing two $N^{3-}$ species. Another structural configuration derived from two O substituting two separated 4-coordinated N from the interstitial one was found to be 3.86 kJ $mol^{-1}$ higher than the lowest-energy structure.

With respect to $Ta_{2.9}N_{4.6}O_{0.4}$, the strong interaction between the Ta-vacancy and the five O was at the origin of its good stability. In the most stable structural configuration, the five O atoms occupying five N sites surround the Ta-vacancy, as displayed in Fig. 3c. The obtained lattice constants are again very similar to those of $Ta_3N_5$ (Table 1). For this structure, the most favorable spin situation is found to be a singlet resulting from five $O^{2-}$ replacing five $N^{3-}$ in conjunction with the five holes released from the created Ta vacancy. Note that the geometrical configuration displaying the well-separated five O and the Ta-vacancy was less stable by 9.16 kJ $mol^{-1}$.

The relative formation energies of the pure materials of $Ta_3N_{4.83}O_{0.17}$, $Ta_3N_{4.83}O_{0.25}$ and $Ta_{2.9}N_{4.6}O_{0.4}$ were computed at 1200 K (typical annealing temperature for these materials) and values of −42.54, −57.62 and −98.60 kJ $mol^{-1}$ were obtained, respectively. As their formation energies are much lower than that of pure $Ta_3N_5$, it can be clearly concluded that the three potential partially O-enriched bulk structures are thermodynamically more stable than the pure material. This result clearly explains the presence of unavoidable O at N sites with Ta vacancies as intrinsic defects in $Ta_3N_5$ samples remaining from $Ta_2O_5$ nitridation methods.[20,23]

For pure $Ta_3N_5$, the computed 2.2 eV band gap well reproduced the measured value (2.1 eV)[23,26,55,56] (Fig. S2, ESI†).

Considering $Ta_3N_{4.83}O_{0.17}$, the electronic structure analysis shows an *n*-type conductivity as observed experimentally,[23,26] which is represented by pinning up the Fermi level near the CBM of $Ta_3N_5$, as shown in Fig. 4a. This phenomenon originates from the newly created donor states made by $Ta^{4+}$ ($5d^1$) orbitals strongly delocalized over the crystal and located in the 0.7 eV range just below the CBM of $Ta_3N_5$. The CBM state is composed of empty $Ta^{5+}$ ($5d^0$) orbitals and the VBM state consists of filled $N^{3-}$ ($2p^6$) orbitals.

For $Ta_3N_{4.83}O_{0.25}$, a very similar band gap and similar absolute VBM/CBM energy positions together with orbital contributions dominated by $N^{3-}$ ($2p^6$)/$Ta^{5+}$ ($5d^0$) were found to those obtained in the case of pure $Ta_3N_5$ (Fig. 4b and Fig. S2, ESI†).

With respect to $Ta_{2.9}N_{4.6}O_{0.4}$, the electronic DOS analysis reveals a slightly broader band gap of 2.3 eV (Fig. 4c) compared with that of the pure material (2.2 eV). Similar to pure $Ta_3N_5$, the CBM state is mainly made by $Ta^{5+}$ ($5d^0$) orbitals and the VBM state is also dominated by occupied $N^{3-}$ ($2p^6$) orbitals due to the minor contributions from $O^{2-}$ ($2p^6$) orbitals in the deeper energy zone of VBM. However, its absolute VBM energy position is shifted downward with respect to that of the pure material one (Fig. 4c and Fig. S2, ESI†) and this is expected to lead to modifications in the redox properties of this material.

Based on the electronic structure results, we focused in what follows on the two relevant partially O-enriched bulk $Ta_3N_5$ structures with substituted O at N sites together with Ta vacancies for deeper surface investigation.

Inside the $Ta_3N_5$ crystalline lattice, four possible crystallographic directions, ⟨110⟩, ⟨100⟩, ⟨010⟩ and ⟨001⟩, are present (Fig. 1). An anisotropic nature is highlighted in the mobility of electrons and holes over the four crystalline orientations of $Ta_3N_{4.83}O_{0.17}$ and $Ta_{2.9}N_{4.6}O_{0.4}$ lattices. The obtained values are reported in Table 2. For electron effective masses, small values of 0.9, 0.7, and 0.7 for $Ta_3N_{4.83}O_{0.17}$ and 0.9, 0.8, and 0.8 for $Ta_{2.9}N_{4.6}O_{0.4}$ are found in the ⟨110⟩, ⟨010⟩ and ⟨001⟩ directions, while greater values of 2.0 and 2.2 are obtained in the ⟨100⟩ orientation, respectively. Consequently, a good mobility for electrons on the (110), (010), and (001) facets and a low mobility

 

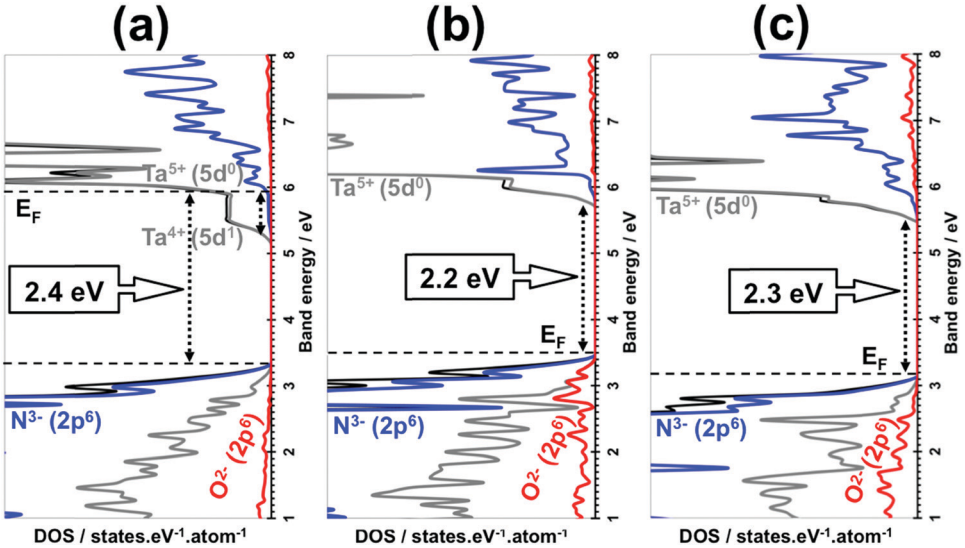


Fig. 4 Electronic density of states (DOS) of the three potential partially O-enriched bulk $Ta_3N_5$ materials obtained using the DFT/HSE06 method: (a) $Ta_3N_{4.83}O_{0.17}$, (b) $Ta_3N_{4.83}O_{0.25}$ and (c) $Ta_{2.9}N_{4.6}O_{0.4}$. Projected DOS is represented by a red curve for O, dark gray for Ta and blue for N. Total DOS is represented by the black curves. CBM and VBM energies are given for each structure. Fermi levels are indicated by black dashed lines.

Table 2 Electron/hole effective masses in different crystalline orientations of the two relevant bulk $Ta_3N_{4.83}O_{0.17}$ and $Ta_{2.9}N_{4.6}O_{0.4}$ crystal lattices

| | $Ta_3N_{4.83}O_{0.17}$ | | $Ta_{2.9}N_{4.6}O_{0.4}$ | |
|---|---|---|---|---|
| Direction | $(m_e^*/m_0)_{ij}$ | $(m_h^*/m_0)_{ij}$ | $(m_e^*/m_0)_{ij}$ | $(m_h^*/m_0)_{ij}$ |
| ⟨110⟩ | 0.9 | 0.7 | 0.9 | 0.8 |
| ⟨100⟩ | 2.0 | 3.6 | 2.2 | 3.9 |
| ⟨010⟩ | 0.7 | 0.9 | 0.8 | 1.0 |
| ⟨001⟩ | 0.7 | 0.9 | 0.8 | 1.0 |

on the (100) surface are expected. Small effective mass values of holes are obtained in the ⟨110⟩, ⟨010⟩ and ⟨001⟩ orientations of 0.7, 0.9, and 0.9 for $Ta_3N_{4.83}O_{0.17}$ and 0.8, 1.0, and 1.0 for $Ta_{2.9}N_{4.6}O_{0.4}$, while greater values of 3.6 and 3.9 are found in the ⟨100⟩ orientation, respectively. Consequently, a good mobility for holes on the (110), (010) and (001) facets and a low mobility on the (100) surface are expected.

The similar trends in the transport properties along the ⟨001⟩ and ⟨010⟩ crystal directions may be understood by the similar N and Ta arrangements in the (001)- and (010)-oriented slab structures with similar Ta–Ta and N–N distances (see Fig. 2c and d for more details). The slight discrepancy in the effective masses along the ⟨110⟩ direction might come from the N and Ta arrangements in the (110)-oriented material structure with longer Ta–Ta and shorter N–N distances (see Fig. 2a). The clear difference in the properties along the ⟨100⟩ lattice direction with greater effective masses might come from the appearance of parallel planes to the (100) surface. They are positioned according to the longer N–N and Ta–Ta distances in the (100)-oriented structure (see Fig. 2b).

### Atomic/electronic surface structures and band alignment for water redox reactions

Four distinctive (110), (100), (010) and (001) low-index Miller exposed facets can be generated on top of the $Ta_3N_5$ crystal (Fig. 2). The structures of (110) and (100) facets consist of 3-coordinated N and 5-coordinated Ta, while that of the (010) facet is made by 2-coordinated N with 5-coordinated Ta and the (001) facet structure reveals 2- and 3-coordinated N with 4-coordinated Ta (Fig. 2). The obtained surface energies are 1.65, 1.45, 1.21 and 1.02 J $m^{-2}$ for the (001), (010), (100) and (110) facets, respectively. The difference is only in the 0.19–0.24 J $m^{-2}$ range, which means that these surfaces might exist in prepared samples of $Ta_3N_5$ and must be considered for deep analysis. Comparing with the principal (023), (310), and (113) surfaces of synthesized $Ta_3N_5$ samples having similar coordination numbers of surface species, very close respective values for (310) and (023) to those of (110) or (100) and (010) are obtained.[57] This tends to provide a competition between these surfaces. In contrast, the (113) surface energy is found to be higher than the (001) one, which means that (113) is a less stable surface than (001). The presence of only 2-coordinated N with 4-coordinated Ta and very few 3-coordinated Ta makes this surface very sensitive.

Regarding the partially O-enriched $Ta_3N_5$, different surfaces were built by replacing with O some of the new 2- or 3-fold sub-coordinated generated surface N and the 3-fold coordinated bulk N sites when Ta vacancies are present inside the lattice to find the most favorable location of O. These four models led to the stoichiometry $Ta_{(3-x)}N_{(5-y)}O_y$ with $x = 0.072$; $y = 0.437$ for (110), $x = 0.072$; $y = 0.50$ for (100), $x = 0.084$; $y = 0.583$ for (010) and $x = 0.084$; $y = 0.583$ for (001). The most favorable structure of the (110) $Ta_{2.928}N_{4.563}O_{0.437}$ slab is found when the 3-fold and 2-fold coordinated O exists in the bulk and surrounding the Ta-vacancy (Fig. 5a). For the (100) $Ta_{2.928}N_{4.5}O_{0.5}$ slab, the most favorable surface structure is partially covered by 3-coordinated O with some 3- and 2-coordinated O inside the bulk located around the Ta-vacancy (Fig. 5b). The most favorable slab structure of (010) $Ta_{2.916}N_{4.417}O_{0.583}$ is fully covered by 2-coordinated O with some minor O content present in the lattice close to the

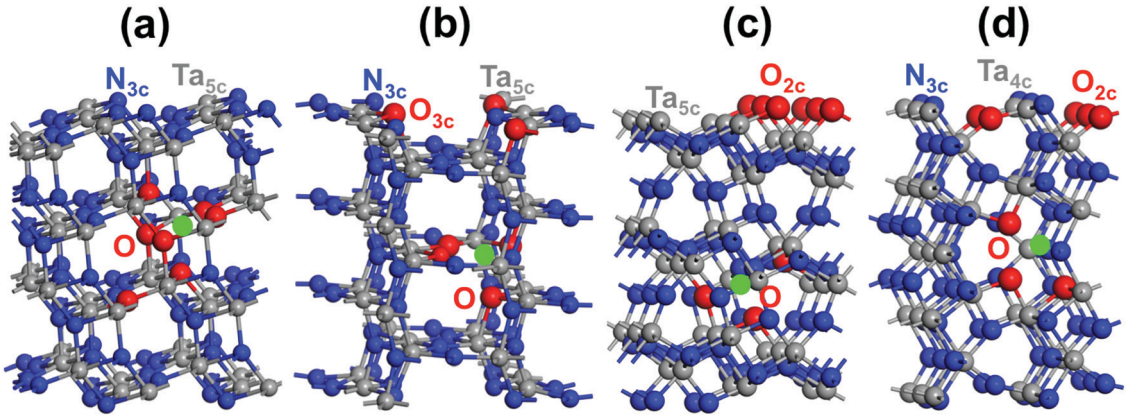


Fig. 5 The most favorable structures of the low-index $Ta_{(3-x)}N_{(5-y)}O_y$ exposed facets: (a) (110) $Ta_{2.928}N_{4.563}O_{0.437}$, (b) (100) $Ta_{2.928}N_{4.5}O_{0.5}$, (c) (010) $Ta_{2.916}N_{4.417}O_{0.583}$ and (d) (001) $Ta_{2.916}N_{4.417}O_{0.583}$. O is shown in red, Ta vacancy is shown in light green, Ta is shown in dark gray and N is shown in blue. For each structure, the coordination numbers of O, N and Ta surface species are highlighted.

Ta-vacancy (Fig. 5c). For the (001) $Ta_{2.916}N_{4.417}O_{0.583}$ slab, the most favorable structure reveals a partially covered surface by 2-coordinated O together with 2- and 3-coordinated O inside the material located around the Ta-vacancy (Fig. 5d). The metastable structure is given in the ESI† (Fig. S3). For the four slab structures, the lowest-energy spin situation is found to be singlet. Bader charge analysis highlighted the appearance of $Ta^{4+}$ that originated from released electrons after the substitution of O for N, in line with the experimental results.[23,26]

The surface formation energy of $Ta_{(3-x)}N_{(5-y)}O_y$ relative to the pure material was computed at 1200 K, which is the typical annealing temperature for this material, and values of −0.18, −0.13, −0.08, −0.07 J $m^{-2}$ were found for the (001), (010), (100), (110) facets. Indeed, the relative difference is very small, only in the 0.01–0.05 J $m^{-2}$ range, which highlights that these surfaces might exist in prepared $Ta_3N_5$ samples and must be considered for deep analysis. As the obtained relative formation energy values of the different surfaces are negative and even lower than those obtained without Ta-vacancies,[57] this confirms, once again from the thermodynamic point of view, the presence of O impurities together with Ta-vacancies in the prepared $Ta_3N_5$ samples.[20,23]

Based on these results, $Ta_{(3-x)}N_{(5-y)}O_y$ facets should be less sensitive than those of $Ta_3N_5$ for oxidation. Having mixed O and N or even only O on the surfaces should lead to greater stability when compared to pure material surfaces.

The original band gaps of the (110), (100), (010) and (001) $Ta_{(3-x)}N_{(5-y)}O_y$ slabs were computed and identical values or 0.1 eV broader or 0.6 eV narrower (Fig. 6) were found in comparison with those obtained for the bulk materials (Fig. 4). The VBM/CBM states consist of $N^{3-}$ ($2p^6$)/$Ta^{5+}$ ($5d^0$) orbitals as found in $Ta_3N_5$, while $O^{2-}$ ($2p^6$) orbitals appear lower in the VB states (see Fig. 6). The analysis of their electronic structures highlights the

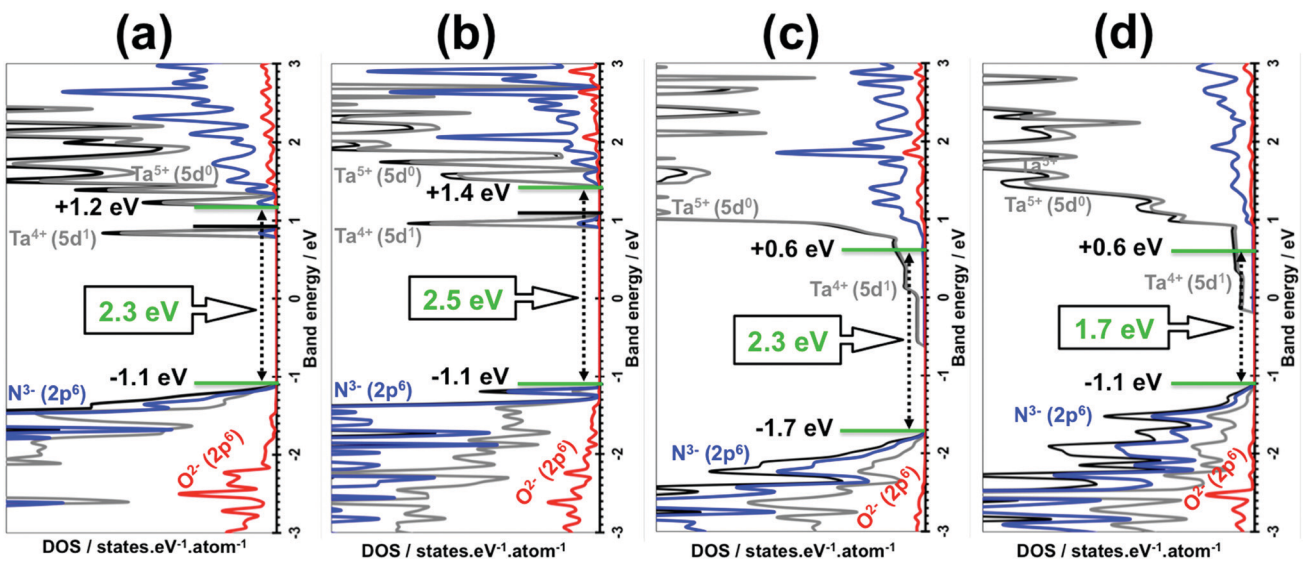


Fig. 6 DFT/HSE06-based density of states (DOS) of $Ta_{(3-x)}N_{(5-y)}O_y$ slabs: (a) (110) $Ta_{2.928}N_{4.563}O_{0.437}$, (b) (100) $Ta_{2.928}N_{4.5}O_{0.5}$, (c) (010) $Ta_{2.916}N_{4.417}O_{0.583}$ and (d) (001) $Ta_{2.916}N_{4.417}O_{0.583}$. Projected DOS is highlighted by the red curve for O, the dark gray curve for Ta and blue for N. Total DOS is highlighted by the black curves. CBM and VBM energies are given in green. Fermi levels are indicated by black lines. For the (010) and (001) facets, the Fermi levels and CBM levels are identical.

appearance of donor states made by $Ta^{4+}$ ($5d^1$) orbitals located in the range of 0.4–1.0 eV lower than the CBM of the original material (see Fig. 6). This result leads to a material with *n*-type conductivity as obtained in experiments.[23,26]

The absolute VBM/CBM energy levels of $Ta_{(3-x)}N_{(5-y)}O_y$ slabs are −1.1/+0.6 eV, −1.7/+0.6 eV, −1.1/+1.4 eV, and −1.1/+1.2 eV, for (001), (010), (100), and (110), respectively, as shown in Fig. 6. Their potential profiles give vacuum energies of 3.9 eV, 4.8 eV, 3.9 eV and 4.5 eV for (001), (010), (100) and (110), respectively, as shown in Fig. 7. The band energy levels of $Ta_{(3-x)}N_{(5-y)}O_y$ slabs are then positioned relative to the vacuum (see the ESI† for more details). An anisotropic nature is highlighted on the basis of exposed facet nature. The VBM energy levels of (001), (100) and (110) slabs are found to be 0.73, 0.73 and 0.13 eV higher than the $O_2/H_2O$ level (see Fig. 8a, b and d). Their CBM energy level is 1.2, 2.0 and 1.2 eV higher than the $H^+/H_2$ level (see Fig. 8a, b and d). In contrast, the (010) VBM level is 0.77 eV below the $O_2/H_2O$ level and the CBM position is 0.3 eV higher than the $H^+/H_2$ potential (Fig. 8c). Due to the inappropriate VBM energy levels of (110), (100) and (001) slabs relative to the $O_2/H_2O$ level, the generated holes on these surfaces will lose the required driving force for water oxidation. Consequently, these surfaces are predicted as suitable candidates only for HER due to their appropriate CBM level with respect to the $H^+/H_2$ level.

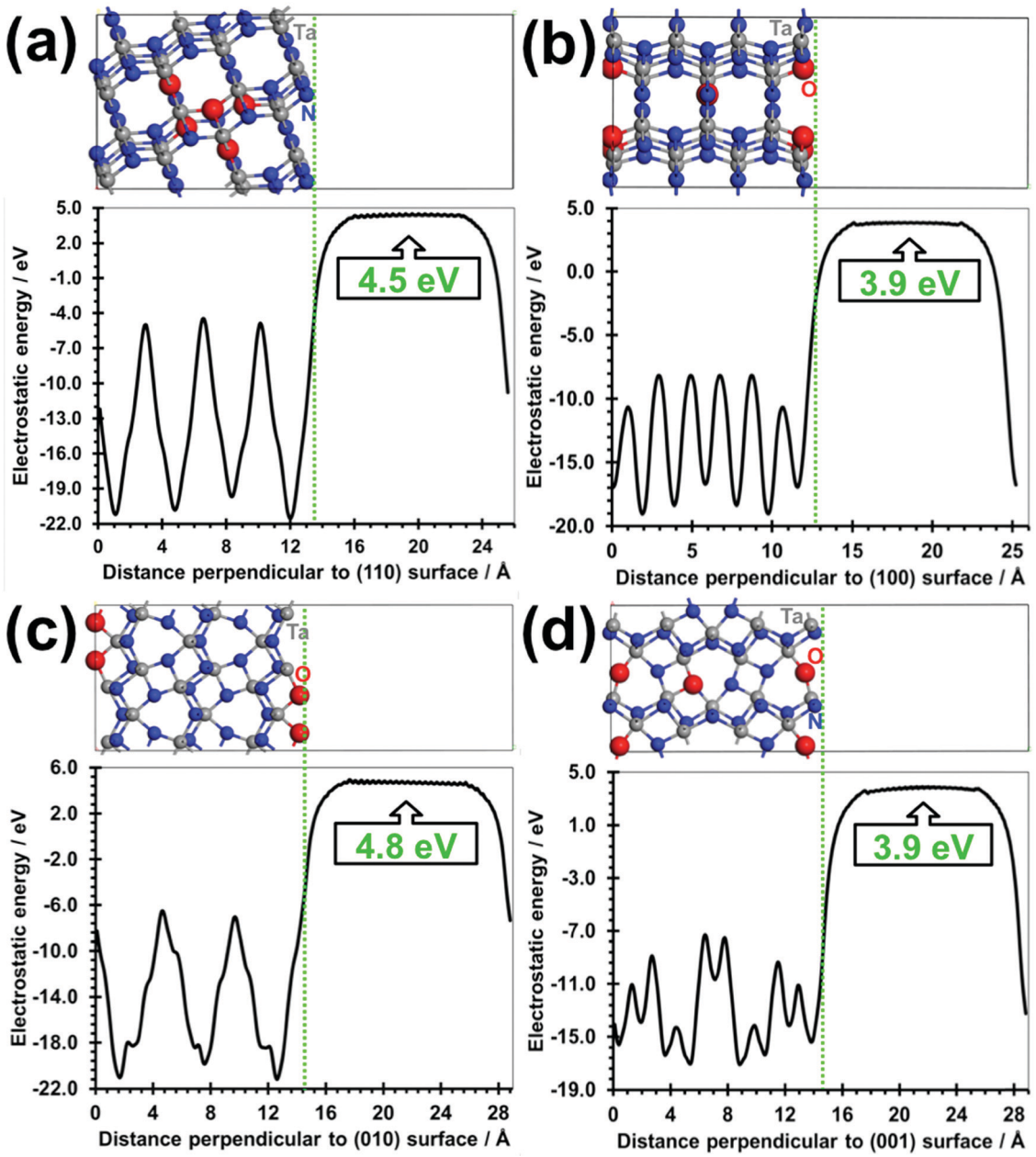


Fig. 7 Local potential profiles for $Ta_{(3-x)}N_{(5-y)}O_y$ slabs obtained using the DFT/HSE06 method: (a) (110) $Ta_{2.928}N_{4.563}O_{0.437}$, (b) (100) $Ta_{2.928}N_{4.5}O_{0.5}$, (c) (010) $Ta_{2.916}N_{4.417}O_{0.583}$ and (d) (001) $Ta_{2.916}N_{4.417}O_{0.583}$. The vacuum energy is given for each exposed facet structure.

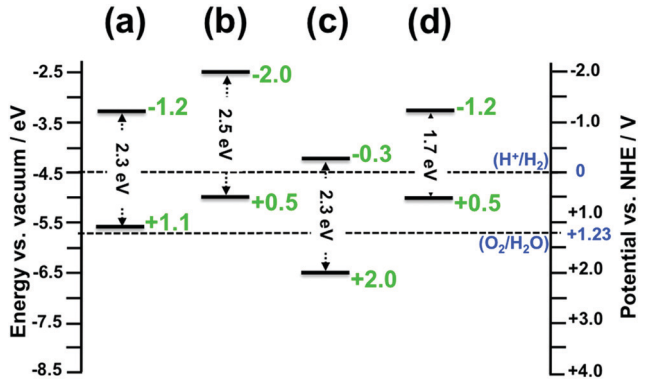


Fig. 8 CBM and VBM energy levels relative to the vacuum for $Ta_{(3-x)}N_{(5-y)}O_y$ slabs obtained using the DFT/HSE06 method: (a) (110) $Ta_{2.928}N_{4.563}O_{0.437}$, (b) (100) $Ta_{2.928}N_{4.5}O_{0.5}$, (c) (010) $Ta_{2.916}N_{4.417}O_{0.583}$ and (d) (001) $Ta_{2.916}N_{4.417}O_{0.583}$. The normal hydrogen electrode (NHE) scale is also displayed for the sake of comparison.

In contrast, as both CBM and VBM levels of the (010) slab are correctly positioned with respect to the $H^+/H_2$ and $O_2/H_2O$ potentials, respectively, this surface is a suitable candidate for HER and OER. Our computed data for the (010) surface are in good agreement with the measurements achieved recently revealing overall water splitting on $Ta_3N_5$ nanorod single crystals grown on the edges of $KTaO_3$ through the (010) surface.[58] Following this result, the ability to oxidize water using this material can be maintained by putting an OER co-catalyst on top of the (010) surface. The similar trend in the redox properties between (100) and (001) surfaces comes from the fact that 4- or 5-coordinated Ta and 3-coordinated N with 2- or 3-coordinated O are present on the two surfaces. Interestingly, the small downward shift in the (110) VBM position can be correlated with the three-fold coordinated N species present on this surface. However, the appearance of only 2-fold coordinated O on the (010) surface may explain the drastic change in its redox features with an important downward shift.

One should be reminded here that very similar electronic and redox properties are obtained for the two (310) and (110) facets and for the two (023) and (010) facets due to the similarities in N and Ta structural distributions on each surface together with the coordination number of surface species.[57] The results presented here highlight the impact of each surface on proton reduction or water oxidation depending on the chemical element structural distribution and the surface species coordination number.

As defined in the introduction, the co-catalysts for $H_2$ and $O_2$ evolution reactions must be, in principle, deposited over promising surfaces to improve the kinetics of electron and hole transfer to water solution. Obtaining such an anisotropic nature in the optoelectronic and redox features makes water splitting more complex.[59,60] Consequently, by merging the optoelectronic and redox properties together, our work indicates the (010) surface as being the only appropriate candidate for OER, whereas the two (110) and (001) $Ta_{(3-x)}N_{(5-y)}O_y$ surfaces are the most appropriate candidates for HER. The 5- and 4-coordinated Ta exposed species would be the active sites for proton reduction towards HER on the two (110) and (001) surfaces, respectively. The 2-coordinated O exposed species would be the active site for water oxidation towards OER on the (010) surface. The increase or decrease in the number of defects is expected to minimally affect the number of active sites and, therefore, the overall activity of the photocatalyst.

Having suitable flat band potentials of $Ta_3N_5$ powder samples relative to water redox limits cannot ensure an active photocatalytic material for water splitting reactions because of the anisotropic behavior of its redox and optoelectronic features and their direct relation with the type/nature of exposed facets. The low efficiency for water splitting obtained so far using this material can be supported by the obtained results from this work. The most effective way to overcome the water splitting efficiency limitation requires a deposition of the co-catalyst for OER on the (010) surface and that for HER either on the (110) or (001) surface.

## Conclusions

We investigated the impact of native defects and exposed facets on the thermodynamic stability, and optoelectronic and redox characteristics of the $Ta_3N_5$ photocatalyst for solar water splitting. This was achieved by applying accurate DFT/HSE06-based first-principles calculations. Among the three explored potential candidates for O-enriched bulk $Ta_3N_5$ structures associated with substituted O species at N sites and accompanied by interstitial O or Ta-vacancies, the first and third structures were relevant. Four possible (001), (010), (100) and (110) low Miller index surfaces for $Ta_{(3-x)}N_{(5-y)}O_y$ ($y = 7x$) were then investigated and they revealed lower formation energies than those of the pure $Ta_3N_5$, which highlights the presence of O at N sites together with Ta vacancies as native defects in the prepared samples. Merging the anisotropic character of the redox and optoelectronic features led to the identification of the promising facets for $H_2$ and $O_2$ evolution reactions.

Our study predicted the two (110) and (001) $Ta_{(3-x)}N_{(5-y)}O_y$ surfaces as being the most appropriate candidates for HER due to appropriate CBM levels with respect to the $H^+/H_2$ level together with good accumulation of photogenerated electrons, whereas the (010) surface was the only appropriate candidate for OER due to its appropriate VBM level with respect to the $O_2/H_2O$ level along with good accumulation of photogenerated holes.

In summary, our work indicates that different facets can have remarkably different photophysico-chemical properties, with an impact on their potential performance in HER and OER. This concept will help experimentalists in choosing the appropriate exposed facets where the HER and OER co-catalysts should be anchored.

## Conflicts of interest

The authors declare no competing financial interest.

## Acknowledgements

This research project was carried out at the King Abdullah University of Science and Technology (KAUST). We warmly

thank the KAUST Supercomputing Laboratory (KSL) for the computational time granted to this work.

## References

1 K. Maeda and K. Domen, *J. Phys. Chem. C*, 2007, **111**, 7851–7861.
2 A. J. Esswein and D. G. Nocera, *Chem. Rev.*, 2007, **107**, 4022–4047.
3 A. Kudo and Y. Miseki, *Chem. Soc. Rev.*, 2009, **38**, 253–278.
4 K. Maeda and K. Domen, *J. Phys. Chem. Lett.*, 2010, **1**, 2655–2661.
5 H. Tong, S. Ouyang, Y. Bi, N. Umezawa, M. Oshikiri and J. Ye, *Adv. Mater.*, 2012, **24**, 229–251.
6 T. Ohno, K. Sarukawa and M. Matsumura, *New J. Chem.*, 2002, **26**, 1167–1170.
7 R. Li, F. Zhang, D. Wang, J. Yang, M. Li, J. Zhu, X. Zhou, H. Han and C. Li, *Nat. Commun.*, 2013, **4**, 1432.
8 J. Yu, J. Low, W. Xiao, P. Zhou and M. Jaroniec, *J. Am. Chem. Soc.*, 2014, **136**, 8839–8842.
9 S. Gao, W. Wang, Y. Ni, C. Lu and Z. Xu, *J. Alloys Compd.*, 2015, **647**, 981–988.
10 C. Li, C. Koenigsmann, W. Ding, B. Rudshteyn, K. P. Yang, K. P. Regan, S. J. Konezny, V. S. Batista, G. W. Brudvig, C. A. Schmuttenmaer and J.-H. Kim, *J. Am. Chem. Soc.*, 2015, **137**, 1520–1529.
11 W. Wang, J. Fang, Y. Zhou, W. Zhang and C. Lu, *RSC Adv.*, 2016, **6**, 67556–67564.
12 W. Li, K. R. Yang, X. Yao, Y. He, Q. Dong, G. W. Brudvig, V. S. Batista and D. Wang, *ACS Appl. Mater. Interfaces*, 2019, **11**, 5616–5622.
13 S. Wang, G. Liu and L. Wang, *Chem. Rev.*, 2019, **119**, 5192–5247.
14 O. Madelung, *Semiconductors: Data Handbook*, Springer, New York, 3rd edn, 2004, pp. 1–691.
15 S. Adashi, *GaAs and Related Materials*, World Scientific Publishing Co. Pvt. Ltd, Singapore, 1994.
16 I. Vurgaftman, J. R. Meyer and L. R. Ram-Mohan, *J. Appl. Phys.*, 2001, **89**, 5815–5875.
17 A. L. Linsebigler, G. Lu and J. T. Yates, *Chem. Rev.*, 1995, **95**, 735–758.
18 M. Hara, G. Hitoki, T. Takata, J. N. Kondo, H. Kobayashi and K. Domen, *Catal. Today*, 2003, **78**, 555–560.
19 W.-J. Chun, A. Ishikawa, H. Fujisawa, T. Takata, J. N. Kondo, M. Hara, M. Kawai, Y. Matsumoto and K. Domen, *J. Phys. Chem. B*, 2003, **107**, 1798–1803.
20 S. J. Henderson and A. L. Hector, *J. Solid State Chem.*, 2006, **179**, 3518–3524.
21 L. Yuliati, J.-H. Yang, X. Wang, K. Maeda, T. Takata, M. Antonietti and K. Domen, *J. Mater. Chem.*, 2010, **20**, 4295–4298.
22 C.-T. Ho, K.-B. Low, R. F. Klie, K. Maeda, K. Domen, R. J. Meyer and P. T. Snee, *J. Phys. Chem. C*, 2010, **115**, 647–652.
23 E. Nurlaela, S. Ould-Chikh, M. Harb, S. del Gobbo, M. Aouine, E. Puzenat, P. Sautet, K. Domen, J.-M. Basset and K. Takanabe, *Chem. Mater.*, 2014, **26**, 4812–4825.
24 M. Harb, P. Sautet and P. Raybaud, *J. Phys. Chem. C*, 2011, **115**, 19394–19404.
25 M. Harb, D. Masih, S. Ould-Chikh, P. Sautet, J.-M. Basset and K. Takanabe, *J. Phys. Chem. C*, 2013, **117**, 17477–17484.
26 M. Harb, P. Sautet, E. Nurlaela, P. Raybaud, L. Cavallo, K. Domen, J.-M. Basset and K. Takanabe, *Phys. Chem. Chem. Phys.*, 2014, **16**, 20548–20560.
27 A. Ziani, M. Harb, D. Noureldine and K. Takanabe, *Appl. Phys. Lett.*, 2015, **3**, 096101.
28 D. Noureldine, S. Lardhi, A. Ziani, M. Harb, L. Cavallo and K. Takanabe, *J. Mater. Chem. C*, 2015, **3**, 12032–12039.
29 S. Lardhi, D. Noureldine, M. Harb, A. Ziani, L. Cavallo and K. Takanabe, *J. Chem. Phys.*, 2016, **144**, 134702.
30 M. Harb and L. Cavallo, *ACS Omega*, 2018, **3**, 18117–18123.
31 J. Heyd, G. E. Scuseria and M. Ernzerhof, *J. Chem. Phys.*, 2003, **118**, 8207–8215.
32 J. Heyd, G. E. Scuseria and M. Ernzerhof, *J. Chem. Phys.*, 2006, **124**, 219906.
33 M. Harb, G. Jeantelot and J.-M. Basset, *J. Phys. Chem. C*, 2019, **123**, 28210–28218.
34 T. Luttrell, S. Halpegamage, J. Tao, A. Kramer, E. Sutter and M. Batzill, *Nat. Sci. Rep.*, 2014, **4**, 4043.
35 A. Sclafani and J. M. Hermann, *J. Phys. Chem.*, 1996, **3654**, 13655–13661.
36 L. Kavan, M. Gratzel, S. E. Gilbert, C. Klemenz and H. J. Scheel, *J. Am. Chem. Soc.*, 1996, **118**, 6716–6723.
37 M. Harb, P. Sautet and P. Raybaud, *J. Phys. Chem. C*, 2013, **117**, 8892–8902.
38 H. Zhu, D. C. Rosenfeld, M. Harb, D. H. Anjum, M. N. Hedhili, S. Ould-Chikh and J.-M. Basset, *ACS Catal.*, 2016, **6**, 2852–2866.
39 J.-W. Jang, D. Friedrich, S. Müller, M. Lamers, H. Hempel, S. Lardhi, Z. Cao, M. Harb, L. Cavallo, R. Heller, R. Eichberger, R. van der Krol and F. F. Abdi, *Adv. Energy Mater.*, 2017, **7**, 1701536.
40 P. E. Blöchl, *Phys. Rev. B: Condens. Matter Mater. Phys.*, 1994, **50**, 17953–17979.
41 J. P. Perdew, K. Burke and M. Ernzerhof, *Phys. Rev. Lett.*, 1996, **77**, 3865–3868.
42 G. Kresse and J. Hafner, *Phys. Rev. B: Condens. Matter Mater. Phys.*, 1994, **49**, 14251–14269.
43 G. Kresse and J. Furthmüller, *Phys. Rev. B: Condens. Matter Mater. Phys.*, 1996, **54**, 11169–11186.
44 G. Kresse and J. Furthmüller, *Comput. Mater. Sci.*, 1996, **6**, 15–50.
45 G. Kresse and D. Joubert, *Phys. Rev. B: Condens. Matter Mater. Phys.*, 1999, **59**, 1758–1775.
46 B. Delley, *J. Chem. Phys.*, 2000, **113**, 7756–7764.
47 B. Delley, *J. Chem. Phys.*, 1990, **92**, 508–517.
48 C. G. Van de Walle and R. M. Martin, *Phys. Rev. B: Condens. Matter Mater. Phys.*, 1987, **35**, 8154–8165.
49 A. Franciosi and C. G. Van de Walle, *Surf. Sci. Rep.*, 1996, **25**, 1–140.
50 J. Rossmeisl, E. Skúlason, M. E. Björketun, V. Tripkovic and J. K. Nørskov, *Chem. Phys. Lett.*, 2008, **466**, 68–71.
51 V. Stevanovic, S. Lany, D. S. Ginley, W. Tumasb and A. Zungerc, *Phys. Chem. Chem. Phys.*, 2014, **16**, 3706–3714.
52 T. A. Pham, Y. Ping and G. Galli, *Nat. Mater.*, 2017, **16**, 401–408.

53 G. Makov and M. C. Payne, *Phys. Rev. B: Condens. Matter Mater. Phys.*, 1995, **51**, 4014–4022.
54 A. Fonari and C. Sutton, Effective Mass Calculator for Semiconductors, http://afonari.com/emc/.
55 M. Harb, L. Cavallo and J.-M. Basset, *J. Phys. Chem. C*, 2014, **118**, 20784–20790.
56 E. Nurlaela, M. Harb, S. del Gobbo, M. Vashishta and K. Takanabe, *J. Solid State Chem.*, 2015, **229**, 219–227.
57 M. Harb and J.-M. Basset, *J. Phys. Chem. C*, 2020, **124**, 2472–2480.
58 Z. Wang, Y. Inoue, T. Hisatomi, R. Ishikawa, Q. Wang, T. Takata, S. Chen, N. Shibata, Y. Ikuhara and K. Domen, *Nat. Catal.*, 2018, **1**, 756–763.
59 H. Wang, L. Qiao, H. Xu, Y. Lin, Y. Shen and C. Nan, *Soft Nanosci. Lett.*, 2016, **6**, 11–30.
60 D. Kim, B. C. Yeo, D. Shin, H. Choi, S. Kim, N. Park and S. S. Han, *Phys. Rev. B*, 2017, **95**, 045209.